

Singlet-Doublet Self-interacting Dark Matter and Radiative Neutrino Mass

Debasish Borah,^{1,*} Manoranjan Dutta,^{2,†} Satyabrata Mahapatra,^{2,‡} and Narendra Sahu^{2,§}

¹*Department of Physics, Indian Institute of Technology Guwahati, Assam 781039, India*

²*Department of Physics, Indian Institute of Technology Hyderabad,
Kandi, Sangareddy 502285, Telangana, India*

Abstract

Self-interacting dark matter (SIDM) with a light mediator is a promising scenario to alleviate the small-scale problems of the cold dark matter paradigm while being consistent with the latter at large scales, as suggested by astrophysical observations. This, however, leads to an under-abundant SIDM relic due to large annihilation rates into mediator particles, often requiring an extension of the simplest thermal or non-thermal relic generation mechanism. In this work, we consider a singlet-doublet fermion dark matter scenario where the singlet fermion with a light scalar mediator gives rise to the velocity-dependent dark matter self-interaction through a Yukawa type attractive potential. The doublet fermion, by virtue of its tiny mixing with the singlet, can be long-lived and can provide a non-thermal contribution to the singlet relic at late epochs, filling the deficit in the thermal relic of singlet SIDM. The light scalar mediator, due to its mixing with the standard model Higgs, paves the path for detecting such SIDM at terrestrial laboratories leading to constraints on model parameters from CRESST-III and XENON1T experiments. Enlarging the dark sector particles by two more singlet fermions and one scalar doublet, all odd under an unbroken \mathbb{Z}_2 symmetry can also explain non-zero neutrino mass in scotogenic fashion.

I. INTRODUCTION

There is ample evidence suggesting the existence of a non-luminous, non-baryonic form of matter in the present Universe, known as the Dark Matter (DM). Satellite-borne experiments like Planck and WMAP, which have measured anisotropies in the cosmic microwave background (CMB) very precisely, predict that DM makes up around one-fourth (26.8%) of the present energy density of the Universe. DM abundance is conventionally expressed as [1]: $\Omega_{\text{DM}}h^2 = 0.120 \pm 0.001$ at 68% CL, where Ω_{DM} is the DM density parameter and $h = \text{Hubble Parameter}/(100 \text{ km s}^{-1}\text{Mpc}^{-1})$ is the reduced Hubble parameter. Similar evidences for DM exist in astrophysical observations at galactic and cluster scales as well [2–4]. Note that the estimate of DM abundance by Planck is based on the standard model of cosmology or the Λ CDM model, which has been very successful in describing the Universe at large scales ($\geq \mathcal{O}(\text{Mpc})$). In Λ CDM model, Λ denotes the cosmological constant or the dark energy component of the Universe, and CDM refers to cold dark matter. Dark matter in Λ CDM model is assumed to be a pressure-less, collision-less fluid that provides the required gravitational potential for structure formation in the early Universe. As no standard model (SM) particle mimics the properties that a DM candidate is expected to have, several beyond standard model (BSM) scenarios have been proposed to explain DM. Amongst different possibilities, the weakly interacting massive particle (WIMP) paradigm has been very popular. A WIMP candidate has mass and interactions in the typical electroweak regime and naturally satisfies

the correct DM relic abundance from its thermal freeze-out. This remarkable coincidence is often referred to as the *WIMP Miracle* [5].

While Λ CDM predictions are in remarkable agreement with large scale structures of the Universe, at small scales, it faces severe challenges from several observations, leading to the core-cusp problem, the problem of missing satellites and the too-big-to-fail problem etc. For recent reviews on these issues and possible solutions, see [6, 7]. One interesting solution to these small-scale anomalies was proposed by Spergel and Steinhardt [8] where they considered self-interacting dark matter (SIDM) as an alternative to conventional collision-less CDM of Λ CDM; see [9, 10] for earlier studies. The self interacting nature of DM is often quantified through the ratio of self-interacting cross-section of SIDM to its mass as $\sigma/m \sim 1 \text{ cm}^2/\text{g} \approx 2 \times 10^{-24} \text{ cm}^2/\text{GeV}$ [11–16]. The advantage of SIDM is that it resolves the small-scale anomalies of the Λ CDM model, yet matches with the CDM halos at large radii consistent with observations. This is because of the significant dependency of self-interacting cross-section on DM velocity. Studies of SIDM simulations suggest that self-interaction is stronger at smaller DM velocities and thus have a large impact on small scale structures while it is in agreement with CDM predictions at larger scales with larger DM velocities [11–14, 17–20]. From a particle physics point of view, such a velocity-dependent self-interaction can be naturally realised in models of DM with a light BSM mediator. If there exists some coupling of this light mediator with SM particles, it ensures thermal equilibrium between the dark sector and the SM bath in the early Universe. The same coupling can also be probed at direct search experiments as well [21, 22]. Several model building efforts have been made to realise such scenarios. For example, see [23–31] and references therein.

Another shortcoming of the SM of particle physics is that it also fails to explain the origin of neutrino mass and mixing, which has been established by the neutrino

*Electronic address: dborah@iitg.ac.in

†Electronic address: ph18resch11007@iith.ac.in

‡Electronic address: ph18resch11001@iith.ac.in

§Electronic address: nsahu@phy.iith.ac.in

oscillation experiments [32, 33]. Within the SM, there is no way for the left-handed neutrinos to couple with the SM Higgs field through a renormalisable operator, as there is no right-handed neutrino field. Therefore, BSM frameworks must be invoked to explain the neutrino mass.

In this paper, in order to accommodate a viable SIDM component of the Universe along with an explanation of tiny neutrino mass, we consider a fermionic singlet-doublet extension of the SM. Singlet-doublet fermion DM models have been well studied in the typical WIMP paradigm [34–61], where the mixing between the singlet and the doublet fermion fields are sizeable. On the contrary, here we consider an extremely small singlet-doublet mixing so that the DM is dominantly composed of the singlet. The self-interaction among the DM is achieved by introducing an additional light scalar field which gives rise to an attractive Yukawa-type potential. Moreover, the light scalar mixes with the SM Higgs and paves a way to detect DM at terrestrial laboratories. The non-zero coupling of the dark matter with the visible sector brings the dark sector to thermal equilibrium. However, the requirement of large self-interaction among DM makes the thermal relic of the singlet to be under-abundant. The small mixing between the singlet and doublet fermions makes the latter long-lived, allowing the doublet to decay back to the singlet DM after the singlet component freezes out, thus fulfilling the relic deficit. We then show that the sub-eV neutrino mass can be generated in a scotogenic setup [62] with the help of SIDM and its heavier counterparts and an additional BSM scalar doublet, all odd under an in-built \mathcal{Z}_2 symmetry.

The paper is organised as follows. In section II, we discuss the model for singlet-doublet dark matter followed by a discussion on the scotogenic setup for neutrino mass generation in section III. This is followed by a discussion on charged lepton flavour violation in section IV. The production and relic density of dark matter is discussed in section V followed by discussion on the dark matter self-interaction in VI. Then we discuss the direct and indirect detection prospects in section VII and VIII respectively. We discuss some collider signatures of the model in section IX and finally conclude in section X.

II. SINGLET-DOUBLET FERMION DARK MATTER WITH SELF-INTERACTIONS

We extend the SM by adding one vector-like fermion doublet $\Psi^T = (\psi^0, \psi^-)$ (with hypercharge $Y = -1$, where we use $Q = T_3 + Y/2$), and three right-handed neutrinos (RHN) N_{R_i} . A discrete \mathcal{Z}_2 symmetry is imposed, under which the doublet Ψ and all three RHNs ($N_{R_i}, i = 1, 2, 3$) are odd, while all SM particles are even. All the newly added particles are also singlet under $SU(3)_c$, i.e. colour neutral. To mediate velocity dependent self-interaction of DM, we add a very light scalar singlet S , even under the \mathcal{Z}_2 symmetry. We

also add a \mathcal{Z}_2 -odd scalar doublet η to generate neutrino mass radiatively, which we will discuss in section III. The quantum numbers of these BSM fields under $SU(3)_c \otimes SU(2)_L \otimes U(1)_Y \otimes \mathcal{Z}_2$ are listed in Table I.

Fields		$SU(3)_C \otimes SU(2)_L \otimes U(1)_Y \otimes \mathcal{Z}_2$			
Fermions	$\Psi = \begin{pmatrix} \psi^0 \\ \psi^- \end{pmatrix}$	1	2	-1	-
	$N_{R_i} (i = 1, 2, 3)$	1	1	0	-
Scalars	$S = \frac{s+u+is'}{\sqrt{2}}$	1	1	0	+
	$\eta = \begin{pmatrix} \eta^+ \\ \frac{\eta^0+i\eta^I}{\sqrt{2}} \end{pmatrix}$	1	2	1	-

TABLE I: Charge assignment of BSM fields under the gauge group $\mathcal{G} \equiv \mathcal{G}_{\text{SM}} \otimes \mathcal{Z}_2$, where $\mathcal{G}_{\text{SM}} \equiv SU(3)_c \otimes SU(2)_L \otimes U(1)_Y$.

The Lagrangian of the model, guided by Table I is given by

$$\begin{aligned} \mathcal{L} = & \mathcal{L}_{\text{SM}} + \bar{\Psi} [i\gamma^\mu (\partial_\mu - ig_2 \frac{\sigma^a}{2} W_\mu^a - ig_1 \frac{Y'}{2} B_\mu)] \Psi \\ & + \overline{N_{R_i}} (i\gamma^\mu \partial_\mu) N_{R_i} - M \bar{\Psi} \Psi - \frac{1}{2} M_{N_{R_i}} \overline{N_{R_i}} (N_{R_i})^c \\ & - y_i \bar{\Psi} \tilde{H} (N_{R_i} + (N_{R_i})^c) - Y_{\alpha i} \bar{L}_\alpha \tilde{\eta} N_{R_i} \\ & - y_\Psi \bar{\Psi} \Psi S - y'_i \overline{N_{R_i}} (N_{R_i})^c S + \text{h.c.} + \mathcal{L}_{\text{scalar}}, \quad (1) \end{aligned}$$

where L, H are lepton and Higgs doublets of the SM while $\mathcal{L}_{\text{SM}}, \mathcal{L}_{\text{scalar}}$ are the SM Lagrangian, complete scalar Lagrangian of the model respectively. The scalar potential involving the new scalar doublet η and the scalar singlet S is given by

$$\begin{aligned} V(H, \eta, S) = & -\mu_H^2 H^\dagger H + \frac{\lambda_H}{2} (H^\dagger H)^2 + \mu_\eta^2 \eta^\dagger \eta + \frac{\lambda_\eta}{2} (\eta^\dagger \eta)^2 \\ & + \lambda_{H\eta} (H^\dagger H) (\eta^\dagger \eta) + \lambda'_{H\eta} (H^\dagger \eta) (\eta^\dagger H) \\ & + \frac{\lambda''_{H\eta}}{2} [(H^\dagger \eta)^2 + (\eta^\dagger H)^2] + \mu_S^2 (S^\dagger S) \\ & + \lambda_S (S^\dagger S)^2 + \mu'_S S^3 + \lambda_{SH} (H^\dagger H) (S^\dagger S), \quad (2) \end{aligned}$$

where the linear terms of singlet scalar S are assumed to be negligible. As shown in the Lagrangian given by Eq. (1), the fermion doublet Ψ being vector-like, has a bare Dirac mass M and all the three right handed neutrinos have bare Majorana mass M_{R_i} . We assume the Yukawa couplings y_i between the doublet and singlet fermions to be very small, typically of the order 10^{-10} . After SM Higgs and the singlet scalar S acquire vacuum expectation values (VEV), the Yukawa term $y_i \bar{\Psi} \tilde{H} N_{R_i}$ induces a Dirac mass, which is, albeit very tiny, thanks to the tiny Yukawa couplings ($y_i \sim 10^{-10}$). So, the effect of the singlet-doublet mixing is negligible and the lightest singlet fermion (N_{R_1}) essentially becomes the DM. The motivation for such tiny Yukawa coupling is that, it makes the doublet Ψ sufficiently long-lived to produce the singlet DM at late epoch via its decay. This brings

the DM relic back to the correct ballpark which is otherwise under-abundant due to strong annihilation into light scalar mediator S . The mixing between the singlet scalar S and the SM Higgs paves a way to detect DM at terrestrial laboratories such as CRESST-III and XENON1T. As we discuss in section III, the scalar doublet η along with the singlet right handed neutrinos which are representing SIDM in our setup, give rise light neutrino masses at one loop level.

III. NEUTRINO MASS

In our setup, the right-handed neutrinos (N_{R_i}), the lightest one of which is the SIDM, are all odd under an imposed \mathcal{Z}_2 symmetry. Therefore, the couplings of N_{R_i} with left-handed leptons via SM Higgs are forbidden. Consequently generation of tiny light neutrino mass at the tree level becomes unfeasible and one needs to resort to radiative scenarios. Then the simplest possibility is to introduce a \mathcal{Z}_2 odd scalar doublet η as given in Eq. (1). As a result, the light neutrino masses can be generated via scotogenic one-loop radiative process proposed by Ma [62]. The relevant terms for neutrino mass generation are identified as the bare mass terms of RHNs and the Dirac Yukawa terms that couple SM lepton doublets and RHNs via scalar doublet η , as shown in Eq. (1). After the electroweak symmetry breaking (EWSB),

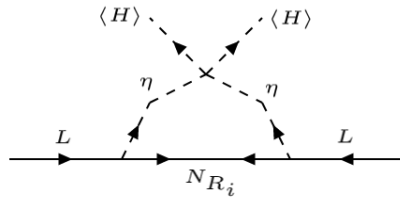


FIG. 1: One-loop generation of light neutrino mass in scotogenic fashion.

the scalar doublets H and η can be parametrised as

$$H = \begin{pmatrix} 0 \\ \frac{v+h}{\sqrt{2}} \end{pmatrix}, \quad \eta = \begin{pmatrix} \eta^\pm \\ \frac{\eta^0 + i\eta^I}{\sqrt{2}} \end{pmatrix}, \quad (3)$$

where v is the vacuum expectation value (VEV) of SM Higgs doublet H , while η does not acquire any VEV to keep the \mathcal{Z}_2 symmetry intact. The neutral scalar (η^0) and pseudoscalar (η^I) acquire masses as follows.

$$M_{R,I}^2 = \mu_\eta^2 + \frac{1}{2}(\lambda_{H\eta} + \lambda'_{H\eta} \pm \lambda''_{H\eta}) v^2, \quad (4)$$

Neutrino mass is induced via the one-loop diagram shown in Fig. 1 and is given by

$$(\mathcal{M}_\nu)_{\alpha\beta} = \sum_{k=1}^3 \frac{(Y)_{i\beta}(Y)_{i\alpha}}{32\pi^2} M_{N_{R_i}} \left[\frac{M_R^2}{M_R^2 - M_{N_{R_i}}^2} \ln \left(\frac{M_R^2}{M_{N_{R_i}}^2} \right) - \frac{M_I^2}{M_I^2 - M_{N_{R_i}}^2} \ln \left(\frac{M_I^2}{M_{N_{R_i}}^2} \right) \right] \quad (5)$$

where $M_{N_{R_i}, i=1,2,3}$ are the mass eigenvalues of the RHN mass eigenstates $N_{R_i}, i = 1, 2, 3$ in the internal line and the indices $\alpha, \beta = e, \mu, \tau$ run over the three neutrino generations. Neutrino mass vanishes in the limit of $\lambda''_{H\eta} \rightarrow 0$ as it corresponds to degenerate neutral scalar and pseudoscalar masses $M_R^2 = M_I^2$. Thus, apart from the Yukawa couplings (Y) and RHN masses, the quartic coupling ($\lambda''_{H\eta}$) also plays a significant role in neutrino mass generation.

To include the constraints from light neutrino data in the analysis, it is often convenient to write the Yukawa couplings in the Casas-Ibarra parametrisation [63, 64] as

$$Y = \sqrt{\Lambda}^{-1} R \sqrt{\hat{m}_\nu} U_{\text{PMNS}}^\dagger \quad (6)$$

where R , in general, is an arbitrary complex orthogonal matrix satisfying $RR^T = I$ that can be parametrised in terms of three complex angles (α, β, γ). We use R equal to the identity matrix (I_3), as considering it to be complex does not alter the DM phenomenology. Here, $\hat{m}_\nu = \text{Diag}(m_1, m_2, m_3)$ is the diagonal light neutrino

mass matrix and the diagonal matrix Λ is defined as $\Lambda = \text{Diag}(\Lambda_1, \Lambda_2, \Lambda_3)$, with

$$\Lambda_i = \frac{2\pi^2}{\lambda_5} \zeta_k \frac{2M_{N_{R_i}}}{v^2},$$

and $\zeta_i = \left(\frac{M_{N_{R_i}}^2}{8(M_R^2 - M_I^2)} [L_i(M_R^2) - L_i(M_I^2)] \right)^{-1}.$ (7)

where

$$L_i(m^2) = \frac{m^2}{m^2 - M_{N_{R_i}}^2} \ln \frac{m^2}{M_{N_{R_i}}^2}. \quad (8)$$

In Eq. (6), U_{PMNS} represents the usual Pontecorvo-Maki-Nakagawa-Sakata (PMNS) mixing matrix of neutrinos.

IV. LEPTON FLAVOR VIOLATION

In the SM, charged lepton flavour violating (CLFV) decays like $\mu \rightarrow e\gamma$ occurs at loop level and is highly suppressed by the smallness of neutrino masses and remains much beyond the current experimental sensitivity [65]. Therefore, any future observation of such LFV decays like $\mu \rightarrow e\gamma$ will definitely be an indication of new physics beyond the SM.

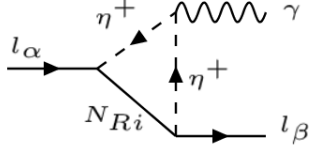


FIG. 2: Feynman diagram of CLFV decay

In the scotogenic scenario, the charged scalar doublet η^+ running in a loop along with singlet fermions can facilitate such CLFV decays, as shown in Fig. 2. This decay width of $\mu \rightarrow e\gamma$ can be calculated as [64, 68],

$$\text{Br}(\mu \rightarrow e\gamma) = \frac{3(4\pi)^3 \alpha}{4G_F^2} |A_D|^2 \text{Br}(\mu \rightarrow e\nu_\mu \bar{\nu}_e), \quad (9)$$

where A_D is given by

$$A_D = \sum_k \frac{(Y)_{ie}^* (Y)_{i\mu}}{16\pi^2} \frac{1}{M_{\eta^+}^2} f(r_i), \quad (10)$$

with $r_i = M_{N_{R_i}}^2 / M_{\eta^+}^2$. $f(x)$ is the loop function given by

$$f(x) = \frac{1 - 6x + 3x^2 + 2x^3 - 6x^2 \log x}{12(1-x)^4}. \quad (11)$$

The most stringent bound on such CLFV decay is from the MEG collaboration on $\text{Br}(\mu \rightarrow e\gamma) < 4.2 \times 10^{-13}$ at 90% confidence level [65].

Another crucial CLFV observable is the three body decay process $\mu \rightarrow 3e$. This branching fraction is given by [64]:

$$\text{Br}(\mu \rightarrow e\bar{e}e) = \frac{3(4\pi)^2 \alpha^2}{8G_F^2} M^2 \text{Br}(\mu \rightarrow e\nu_\mu \bar{\nu}_e) \quad (12)$$

where details of M^2 is given in the Appendix. E.

Similarly, the conversion of $\mu \rightarrow e$ in nuclei might become one of the most severely constrained CLFV observables in scotogenic scenarios because of the great projected sensitivities of various collaborations. The conversion rate, relative to the the muon capture rate, can be expressed as:

$$\text{CR}(\mu \rightarrow e, \text{Nucleus}) = \frac{p_e E_e m_\mu^3 G_F^2 \alpha_{\text{em}}^3 Z_{\text{eff}}^4 F_p^2}{8\pi^2 Z} K^2 \frac{1}{\Gamma_{\text{capt}}} \quad (13)$$

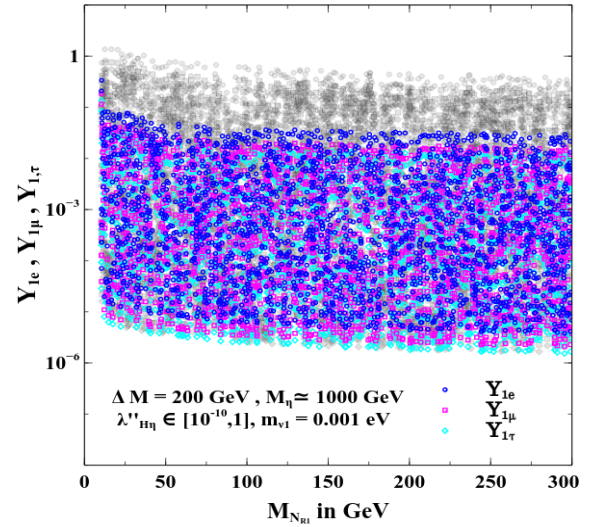


FIG. 3: Yukawa couplings obtained by the Casas-Ibarra parametrisation shown against $M_{N_{R_1}}$. The coloured dots (blue, magenta and cyan) are allowed from all CLFV constraints while the grey coloured points which do not overlap with the colored points are ruled out.

where Z and N are the number of protons and neutrons in the nucleus, Z_{eff} is the effective atomic charge, F_p is the nuclear matrix element and Γ_{capt} represents the total muon capture rate. Furthermore, p_e and E_e (taken to be $\simeq m_\mu$ in the numerical evaluation) are the momentum and energy of the electron and m_μ is the muon mass. The details of K^2 can be found in Appendix F.

In Fig. 3, the N_{R_1} Yukawa couplings obtained by the Casas-Ibarra parametrisation are shown against the mass of N_{R_1} . The coloured dots (blue, magenta and cyan) are allowed from CLFV bounds for $\mu \rightarrow e\gamma$, $\mu \rightarrow 3e$ and $\text{CR}(\mu \rightarrow e : \text{Ti})$ [65–67], while the grey coloured points which do not overlap with the coloured points are ruled out by the CLFV constraints. For the scan, we have fixed the mass splitting between the RHNs ($\Delta M = M_{N_{R_{2,3}}} - M_{N_{R_1}}$) at 200 GeV and M_{η^+} is fixed around 1000 GeV. The $\lambda''_{H\eta}$ coupling, crucial for neutrino mass generation as well as determining the order of Yukawa coupling, is varied randomly in a range $[10^{-10}, 1]$. We consider the normal ordering and the lightest active neutrino mass is assumed to be 10^{-3} eV consistent with the constraint for the sum of active neutrino masses $\sum m_\nu = 0.12$ eV from cosmological data [1]. From Fig. 3, we see that the required $\bar{L}\tilde{\eta}N_{R_i}$ coupling- $Y_{\alpha i}$ roughly varies in the range $10^{-6} - 0.1$ in order to reproduce the correct light neutrino masses and mixing. We will use this information in section V for calculating the relic density of SIDM.

V. PRODUCTION OF SIDM

Due to electroweak gauge interactions, the vector-like fermion doublet Ψ remains in thermal equilibrium at a

temperature above its mass scale in the early Universe. The SM gauge singlets (N_{R_i}), also come to thermal equilibrium through the process $\Psi\Psi \xrightarrow{S} N_{R_i}N_{R_i}$ (shown in the left panel of Fig. 4) mediated by the light scalar S . This is because of the large Yukawa coupling: $y'_i \sim 0.35$ which is necessary for sufficient self interaction as discussed in section VI. Due to efficient annihilation of the dark matter into light scalar S through the process shown in the right panel of Fig. 4, the thermal relic of the DM (N_{R_1}) is found to be under-abundant. The annihilation of a fermion pair through a scalar mediator (irrespective of the final states) is a p-wave process and hence velocity suppressed [69]. The thermally averaged cross-section for the most dominant annihilation process relevant to DM freeze-out is given by:

$$\langle\sigma v\rangle_{\text{DM DM}\rightarrow S} = \frac{3}{4} \frac{y'^4}{16\pi M_{\text{DM}}^2} v^2 \sqrt{1 - \frac{M_S^2}{M_{\text{DM}}^2}} \quad (14)$$

where $M_{\text{DM}} = M_{N_{R_1}}$.

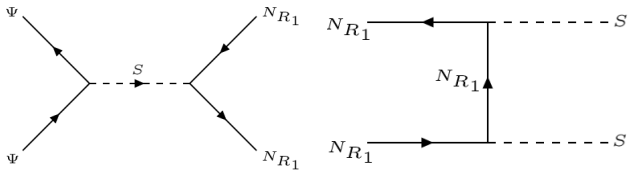


FIG. 4: Left: Feynman diagram responsible for bringing DM into thermal equilibrium, Right: Dominant annihilation mode for DM.

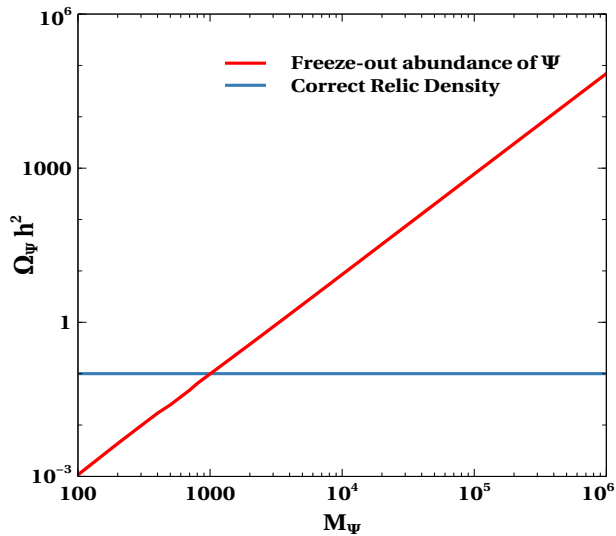


FIG. 5: Freeze-out abundance of Ψ as a function of its mass M_Ψ .

The thermal relic of DM N_{R_1} is under-abundant up to DM mass ~ 1 TeV due to large annihilation cross-section into light mediators given by Eq. (14). Thanks to the small Yukawa coupling of the Lagrangian term $y_i \Psi \tilde{H} N_{R_i}$, the doublet Ψ decays sufficiently late into SM Higgs and the three singlets (N_{R_i}), and since the heavier singlets $N_{R_{2,3}}$ also decay into the DM N_{R_1} eventually, it helps in restoring the DM relic within the correct ballpark.

In the early Universe, the number density of the doublet Ψ gets depleted in three ways *viz.* $\Psi\Psi \rightarrow SS$, $\Psi\Psi \rightarrow N_{R_i}N_{R_i}$ and $\Psi\Psi \rightarrow \text{SM SM}$. Here we assume the Yukawa coupling y_Ψ of the doublet Ψ with light scalar S to be sufficiently small, so that $\Psi\Psi \rightarrow \text{SM SM}$ always dominantly decides the freeze-out abundance of Ψ . Considering $\Psi\Psi \rightarrow \text{SM SM}$ to be the dominant process, the freeze-out number density of Ψ can be easily calculated by implementing SM + inert fermion doublet (Ψ) model in LanHEP [80] and feeding the model files into MicrOmegas [81]. The freeze-out abundance of Ψ as a function of mass M_Ψ is shown in Fig. 5. The relevant interactions for the fermion doublet in component form are shown in Appendix-A. From Fig. 5, we see that freeze-out abundance of Ψ matches the correct relic density ($\Omega_{\text{DM}} h^2 = 0.12$) only for mass around 1000 GeV. Since it is essentially the number density of Ψ that is converted into number density of the DM at late epoch, to produce correct relic for DM N_{R_1} , the freeze-out number density of Ψ must satisfy

$$\Omega_{\text{DM}} h^2 = \left(\frac{M_{\text{DM}}}{M_\Psi}\right) \Omega_\Psi h^2 \quad (15)$$

Note that the inert scalar doublet η also has Yukawa coupling to N_{R_i} . Depending upon the mass hierarchies of η and $N_{R_{2,3}}$, one can decay into other, and this may affect the DM relic density because all \mathbb{Z}_2 odd particles will ultimately decay into DM. To obtain the relic density precisely, we need to solve the relevant coupled Boltzmann equations. We consider two different scenarios depending upon masses of η and $N_{R_{2,3}}$.

Case-I: $M_{N_{R_{2,3}}} < M_\eta < M_\Psi$. In this case, η can decay into all three N_{R_i} with corresponding partial decay width $\Gamma_{\eta \rightarrow N_{R_i} l}$. Thermally produced $N_{R_{2,3}}$ along with those produced from decays of Ψ and η will subsequently decay into DM through the three body decay process $\Gamma(N_{R_{2,3}} \rightarrow N_{R_1} ll)$. Both these processes are simultaneously constrained from charged lepton flavour violation discussed in section IV. The relevant Boltzmann equation in this case is given by Eq. (16) below while the formulae for relevant cross-section and the decay widths are given in Appendix C.

$$\begin{aligned}
\frac{dY_{N_{R_1}}}{dx} &= -\frac{s(M_{\text{DM}})}{x^2 H(M_{\text{DM}})} (\langle \sigma(N_{R_1} N_{R_1} \rightarrow SS)v \rangle) (Y_{N_{R_1}}^2 - (Y_{N_{R_1}}^{\text{eq}})^2) + \frac{x}{H(M_{\text{DM}})} (\langle \Gamma_{\Psi \rightarrow H N_{R_1}} \rangle Y_{\Psi} + \langle \Gamma_{\eta \rightarrow N_{R_1} l} \rangle Y_{\eta}) \\
\frac{dY_{N_{R_{2,3}}}}{dx} &= -\frac{s(M_{\text{DM}})}{x^2 H(M_{\text{DM}})} (\langle \sigma(N_{R_{2,3}} N_{R_{2,3}} \rightarrow SS)v \rangle) (Y_{N_{R_{2,3}}}^2 - (Y_{N_{R_{2,3}}}^{\text{eq}})^2) \\
&\quad + \frac{x}{H(M_{\text{DM}})} (\langle \Gamma_{\Psi \rightarrow H N_{R_{2,3}}} \rangle Y_{\Psi} + \langle \Gamma_{\eta \rightarrow N_{R_{2,3}} l} \rangle Y_{\eta} + \langle \Gamma_{N_{R_{2,3}} \rightarrow N_{R_1} l} \rangle Y_{N_{R_{2,3}}}) \\
\frac{dY_{\Psi}}{dx} &= -\frac{s(M_{\text{DM}})}{x^2 H(M_{\text{DM}})} (\langle \sigma(\Psi\Psi \rightarrow \text{SMSM})v \rangle + \langle \sigma(\Psi\Psi \rightarrow N_R N_R)v \rangle + \langle \sigma(\Psi\Psi \rightarrow SS)v \rangle) (Y_{\Psi}^2 - (Y_{\Psi}^{\text{eq}})^2) \\
&\quad - \frac{x}{H(M_{\text{DM}})} (\langle \Gamma_{\Psi \rightarrow H N_{R_i}} \rangle Y_{\Psi}) \\
\frac{dY_{\eta}}{dx} &= -\frac{s(M_{\text{DM}})}{x^2 H(M_{\text{DM}})} (\langle \sigma(\eta\eta \rightarrow HH)v \rangle) (Y_{\eta}^2 - (Y_{\eta}^{\text{eq}})^2) - \frac{x}{H(M_{\text{DM}})} (\langle \Gamma_{\eta \rightarrow N_{R_i}} \rangle Y_{\eta})
\end{aligned} \tag{16}$$

In the above $x = \frac{M_{\text{DM}}}{T}$, $s(M_{\text{DM}}) = \frac{2\pi^2}{45} g_{*s} M_{\text{DM}}^3$, $H(M_{\text{DM}}) = 1.67 g_*^{1/2} \frac{M_{\text{DM}}^2}{M_{\text{Pl}}}$ and $\langle \sigma(\Psi\Psi \rightarrow \text{SMSM})v \rangle$ represents the thermally averaged cross-section [82] of annihilation of Ψ to all SM particles, which is fixed by the SM gauge interaction of the doublet Ψ . Also $\langle \Gamma_{A \rightarrow BCD} \rangle$ represents the thermally averaged decay width of the process $A \rightarrow BCD$ in general.

Case-II: $M_{\eta} < M_{N_{R_{2,3}}} < M_{\Psi}$. In this case, $N_{R_{2,3}}$ can decay into η through $\Gamma(N_{R_{2,3}} \rightarrow \eta l)$ and η then decays into the DM through the process $\eta \rightarrow N_{R_1} l$, constrained by charged lepton flavour violation. The relevant Boltzmann equations in this case are given by Eq. (17) below.

$$\begin{aligned}
\frac{dY_{N_{R_1}}}{dx} &= -\frac{s(M_{\text{DM}})}{x^2 H(M_{\text{DM}})} (\langle \sigma(N_{R_1} N_{R_1} \rightarrow SS)v \rangle) (Y_{N_{R_1}}^2 - (Y_{N_{R_1}}^{\text{eq}})^2) + \frac{x}{H(M_{\text{DM}})} (\langle \Gamma_{\Psi \rightarrow H N_{R_1}} \rangle Y_{\Psi} + \langle \Gamma_{\eta \rightarrow N_{R_1} l} \rangle Y_{\eta}) \\
\frac{dY_{N_{R_{2,3}}}}{dx} &= -\frac{s(M_{\text{DM}})}{x^2 H(M_{\text{DM}})} (\langle \sigma(N_{R_{2,3}} N_{R_{2,3}} \rightarrow SS)v \rangle) (Y_{N_{R_{2,3}}}^2 - (Y_{N_{R_{2,3}}}^{\text{eq}})^2) + \frac{x}{H(M_{\text{DM}})} (\langle \Gamma_{\Psi \rightarrow H N_{R_{2,3}}} \rangle Y_{\Psi} - \langle \Gamma_{N_{R_{2,3}} \rightarrow \eta l} \rangle Y_{N_{R_{2,3}}}) \\
\frac{dY_{\Psi}}{dx} &= -\frac{s(M_{\text{DM}})}{x^2 H(M_{\text{DM}})} (\langle \sigma(\Psi\Psi \rightarrow \text{SMSM})v \rangle + \langle \sigma(\Psi\Psi \rightarrow N_R N_R)v \rangle + \langle \sigma(\Psi\Psi \rightarrow SS)v \rangle) (Y_{\Psi}^2 - (Y_{\Psi}^{\text{eq}})^2) \\
&\quad - \frac{x}{H(M_{\text{DM}})} (\langle \Gamma_{\Psi \rightarrow H N_{R_i}} \rangle Y_{\Psi}) \\
\frac{dY_{\eta}}{dx} &= -\frac{s(M_{\text{DM}})}{x^2 H(M_{\text{DM}})} (\langle \sigma(\eta\eta \rightarrow HH)v \rangle) (Y_{\eta}^2 - (Y_{\eta}^{\text{eq}})^2) + \frac{x}{H(M_{\text{DM}})} (\langle \Gamma_{N_{R_{2,3}} \rightarrow \eta l} \rangle Y_{N_{R_{2,3}}} - \langle \Gamma_{\eta \rightarrow N_{R_1} l} \rangle Y_{\eta})
\end{aligned} \tag{17}$$

We show the relic density evolution plots for case-I and case-II in the top and bottom panels of Fig. 6 for $M_{\text{DM}} = 100$ GeV, $M_{\Psi} = 12$ TeV, which yield correct relic density of the DM. For better understanding, we show in Fig. 6, the contributions from different subprocesses to the relic abundance in different colour codes as indicated in the figure inset. The evolution of number densities of Ψ , η , $N_{R_{2,3}}$ and the DM in light of all the processes incorporated in the Boltzmann equations given by Eq. (16), Eq. (17) are shown in blue, orange, brown and red coloured curves respectively. Additionally, we have also shown the equilibrium distribution of Ψ , η , $N_{R_{2,3}}$ and the DM in green, magenta, cyan and purple coloured curves respectively and the under-abundant

thermal freeze-out relic of DM is depicted by the dotted dark-cyan curve. Due to the large decay width of η , it decays while still in equilibrium ($\eta \rightarrow N_{R_i} l$) which is too early to mark any significant effect in the final relic of DM N_{R_1} .

In case-I (top panel of Fig. 6), the processes $\eta \rightarrow N_{R_i} l$ and $N_{R_{2,3}} \rightarrow N_{R_1} ll$ are simultaneously constrained from charged lepton flavour violation as the same couplings are involved in all the processes. We consider $M_{\eta} = 1000$ GeV and $M_{N_{R_{2,3}}} = 300$ GeV where the masses of $N_{R_{2,3}}$ are assumed to be equal for simplicity. Then, for $\lambda''_{H\eta} = \mathcal{O}(1)$ and assuming normal hierarchy of active neutrinos, the allowed Yukawa coupling $Y_{i\alpha}$ is of the order $\mathcal{O}(10^{-5})$. The decay width corresponding to this

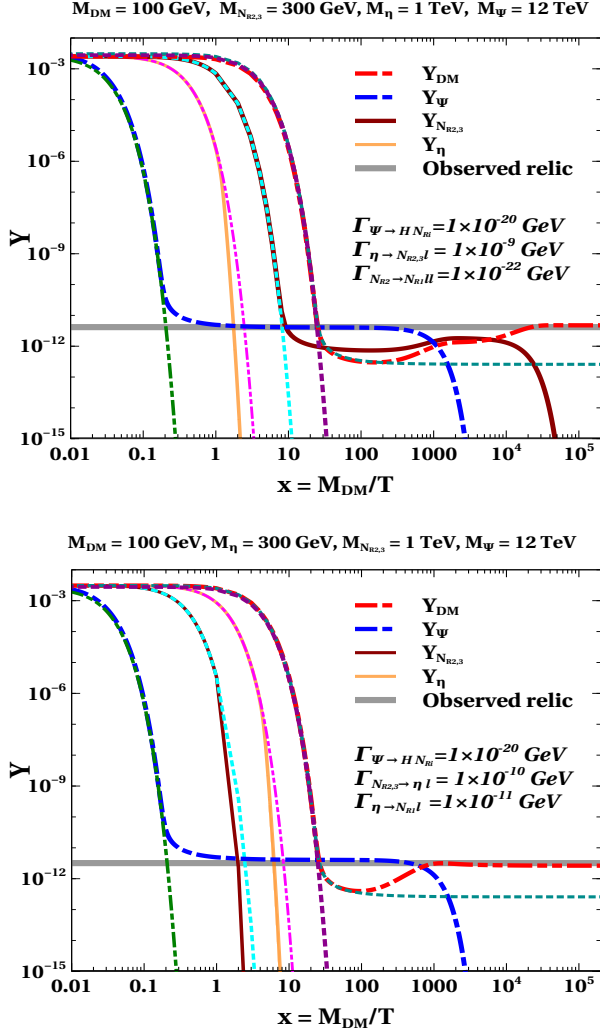


FIG. 6: Evolution of co-moving number densities of dark matter along with other dark sector particles.

coupling is calculated to be $\Gamma_{\eta \rightarrow N_{R_i} l} \simeq 1 \times 10^{-9}$ GeV. Due to such large decay width, η decays while in equilibrium and DM produced at such an early epoch annihilates into light mediators quickly. Therefore, η does not affect DM relic density. The three body decay width of two heavier singlets $N_{R_{2,3}}$ for the same parameter space considered in $\eta \rightarrow N_i l$ is given by $\Gamma_{N_{R_{2,3}} \rightarrow N_{R_1} l l} \simeq 1 \times 10^{-22}$ GeV. Since the decay width of $N_{R_{2,3}}$ is comparable to that of $\Gamma_{\Psi \rightarrow H N_{R_i}}$, its effect can be seen in the plot shown in Fig. 6. The decay of Ψ with decay width $\Gamma_{\Psi \rightarrow H N_{R_i}} = 1 \times 10^{-20}$ GeV produces all N_{R_i} 's equally around $x \sim 2 \times 10^3$ and finally $N_{R_{2,3}}$ decays into the DM (N_{R_1}) around $x \sim 2 \times 10^4$, producing correct final relic density for the dark matter. Note that considering inverted hierarchy of active neutrinos does not alter the consequences significantly. In case-II (bottom panel of Fig. 6), for $\lambda''_{H\eta} = \mathcal{O}(1)$ and normal hierarchy, and masses $M_\eta = 300$ GeV and $M_{N_{R_{2,3}}} = 1000$ GeV, the decay

widths are calculated to be $\Gamma_{N_{R_{2,3}} \rightarrow \eta l} \simeq 1 \times 10^{-10}$ GeV and $\Gamma_{\eta \rightarrow N_{R_1} l} \simeq 1 \times 10^{-11}$ GeV. Due to such large decay widths, both η and $N_{R_{2,3}}$ decays while still in equilibrium, not affecting the final DM relic at all. The correct relic of DM is entirely decided by late decay of Ψ with $\Gamma_{\Psi \rightarrow H N_{R_i}} = 1 \times 10^{-20}$ GeV.

As we can see from Fig. 6, due to the constraints from charged lepton flavour violation, the decay processes other than $\Psi \rightarrow H N_{R_i}$ do not affect the relic significantly and the relation given by Eq. (15) holds for correct DM relic. Thanks to the validity of Eq. (15) and the fact that $\Omega_\Psi h^2$ is decided entirely by M_Ψ , only a certain combination of (M_{DM}, M_Ψ) will produce the correct relic density for the DM. We show in Fig. 7, the contour of correct DM relic density in the plane of M_Ψ versus M_{DM} . As we can see, to obtain the correct relic density for a light DM (below 10 GeV), M_Ψ must be very heavy (above 150 TeV) as expected from Eq. (15). As M_{DM} increases, M_Ψ decreases satisfying Eq. (15) and for $M_{DM} = 300$ GeV, the corresponding $M_\Psi = 3$ TeV. For $M_{DM} \sim 1$ TeV, the relic density in the correct ballpark can directly be satisfied from its thermal freeze-out, beyond which thermal DM relic is over-abundant.

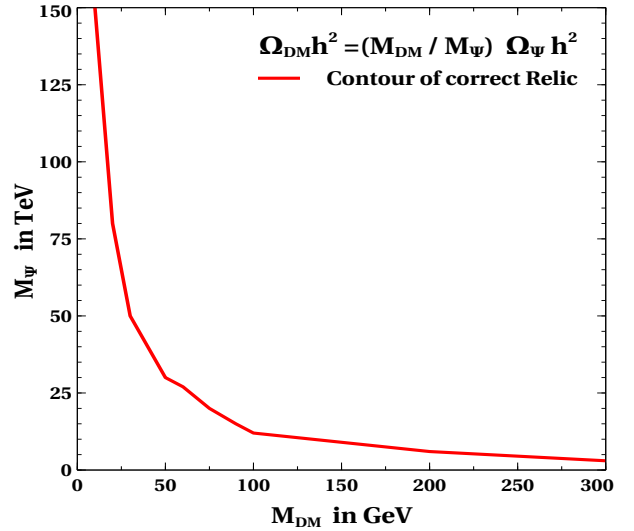


FIG. 7: Contour of correct relic density for the DM (N_{R_1}) in the plane of M_Ψ and M_{DM} .

VI. DARK MATTER SELF-INTERACTION

The dark sector particles have elastic self-scattering through t-channel processes due to the presence of the term $y'_1 \overline{N_{R_1}} (N_{R_1})^c S$ in the model Lagrangian given by Eq. (1). The Feynman diagram of such process is shown in Fig. 8. In order to alleviate the small-scale anomalies of Λ CDM, the typical DM self-scattering cross-section should be $\sigma \sim 1$ cm²/g $\approx 2 \times 10^{-24}$ cm²/GeV, which is 14 orders of magnitude larger than the typical WIMP cross-section ($\sigma \sim 10^{-38}$ cm²/GeV). This suggests the

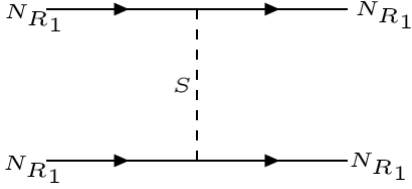


FIG. 8: Feynman diagram for elastic DM self-interaction.

existence of a light mediator, which is much lighter than electroweak scale. The scalar mediator S in our model serves this purpose. The non-relativistic DM scattering can be well described by the attractive Yukawa potential,

$$V(r) = \frac{y_1'^2}{4\pi r} e^{-M_S r} \quad (18)$$

To capture the relevant physics of forward scattering divergence, the transfer cross-section σ_T is defined as [6, 12, 20]

$$\sigma_T = \int d\Omega (1 - \cos\theta) \frac{d\sigma}{d\Omega} \quad (19)$$

Capturing the whole parameter space requires the calculations to be carried out well beyond the perturbative limit. Depending on the masses of DM (M_{DM}) and the mediator (M_S) along with relative velocity of DM (v) and interaction strength ($y_1'^2$), three distinct regimes can be identified, namely the Born regime ($y_1'^2 M_{DM}/(4\pi M_S) \ll 1, M_{DM}v/M_S \geq 1$), classical regime ($y_1'^2 M_{DM}/(4\pi M_S) \geq 1, y_1'^2 M_{DM}/4\pi M_S \geq 1$) and the resonant regime ($y_1'^2 M_{DM}/(4\pi M_S) \geq 1, M_{DM}v/M_S \leq 1$). DM self-scattering cross-section in all three regimes are given in Appendix B. Using these self-interaction cross sections and constraining σ/M_{DM} in the required range from astrophysical observations at different scales, we get the allowed parameter space of the model for sufficient self-interaction in the plane of DM mass M_{DM} and mediator mass M_S . In Fig. 9 and Fig. 10, we show the parameter space for the model in M_{DM} versus M_S plane which gives rise to the required DM self-scattering cross-section (σ/M_{DM}) in the range 0.1 – 1 cm^2/g for clusters ($v \sim 1000$ km/s), 0.1 – 10 cm^2/g for galaxies ($v \sim 200$ km/s) and 0.1 – 100 cm^2/g for dwarf galaxies ($v \sim 10$ km/s). We have also varied the Yukawa coupling y_1' in the range 0.1-1 (shown in coloured bar) which decides the strength of self-scattering.

The allowed region towards the left (right) corner corresponds to the Born(classical) region, where the velocity dependence of the cross-sections are trivial. The central region sandwiched between these two is the resonant region, where quantum mechanical resonances and anti-resonance appear due to the attractive potential. The resonant regime covers a large region of parameter space in the M_{DM} versus M_S plane. These resonances are more prominent at dwarf and galactic scales where DM velocities are comparatively smaller. This is because, for a

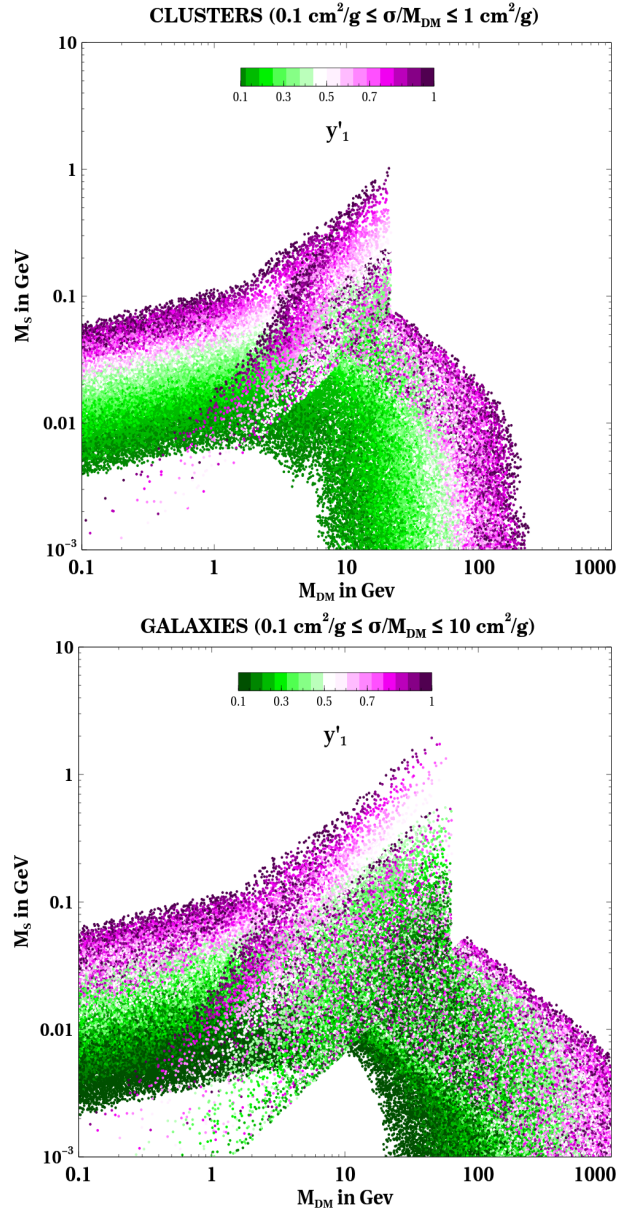


FIG. 9: Top panel: Cluster; Bottom panel: Galaxy; Self-interaction cross-section in the range 0.1–1 cm^2/g for clusters ($v \sim 1000$ km/s) and 0.1 – 10 cm^2/g for galaxies ($v \sim 200$ km/s.)

fixed Yukawa coupling y_1' , the condition $M_{DM}v/M_S < 1$ dictates the onset of non-perturbative quantum mechanical effects is easily satisfied by smaller velocities. The resonant spikes are not distinct in these figures as we have varied the Yukawa coupling in a range 0.1-1. Nevertheless, prominent resonant spikes can be seen in Fig. 14 in section VII, where we show the same parameter space for a fixed Yukawa coupling $y_1' = 0.35$, while confronting the SIDM parameter space to direct search. We can see from the figures that a wide range of DM mass can give rise to sufficient self-interaction. However, the mass of the mediator is constrained roughly within two orders of

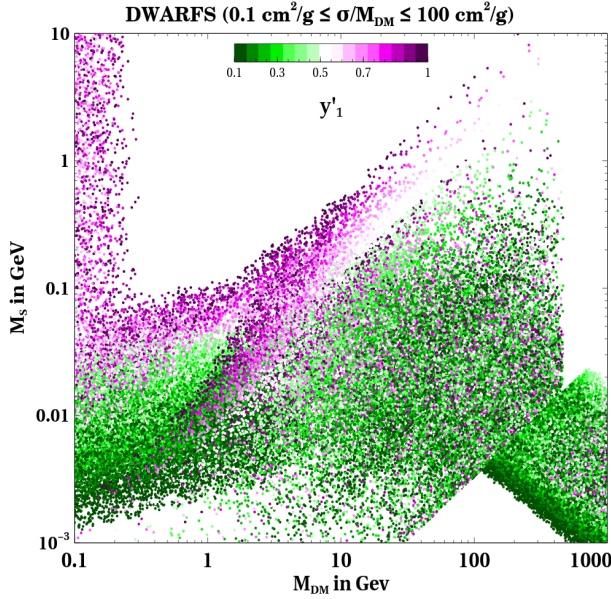


FIG. 10: Self-interaction cross-section in the range $0.1 - 100 \text{ cm}^2/\text{g}$ for dwarfs ($v \sim 10 \text{ km/s}$).

magnitudes excepting for the resonance case.

The self-scattering cross-section per unit DM mass as a function of average collision velocity is shown in figure 11, which fits to data from dwarfs (orange), low surface brightness (LSB) galaxies (blue), and clusters (green) [18, 83]. The red dashed curve corresponding to the velocity-dependent cross-section calculated from our model for a benchmark point (i.e $M_{\text{DM}} = 50 \text{ GeV}$, $M_S = 50 \text{ MeV}$ and $y'_1 = 0.4$), which is allowed from all relevant phenomenological constraints, gives a nice fit to the astrophysical observations. It is clear from the Fig. 11 that the model shows remarkable velocity dependence in self-scattering and can appreciably explain the astrophysical observation of velocity-dependent DM self-interaction.

VII. DIRECT DETECTION

The spin-independent elastic scattering of DM is possible through $S - H$ mixing (θ_{SH}), where DM particles can scatter off the target nuclei which are located at terrestrial laboratories. The Feynmann diagram for direct detection is shown in Fig. 12 and the scattering cross-section of DM per nucleon can be expressed as

$$\sigma_{SI}^{S-H} = \frac{\mu_r^2}{4\pi A^2} [Z f_p + (A - Z) f_n]^2 \quad (20)$$

where $\mu_r = \frac{M_{\text{DM}} m_n}{M_{\text{DM}} + m_n}$ is the reduced mass of the DM-nucleon system, m_n being the nucleon (proton or neutron) mass, A and Z are the mass and atomic number of the target nucleus respectively. The f_p and f_n are the interaction strengths of proton and neutron with DM,

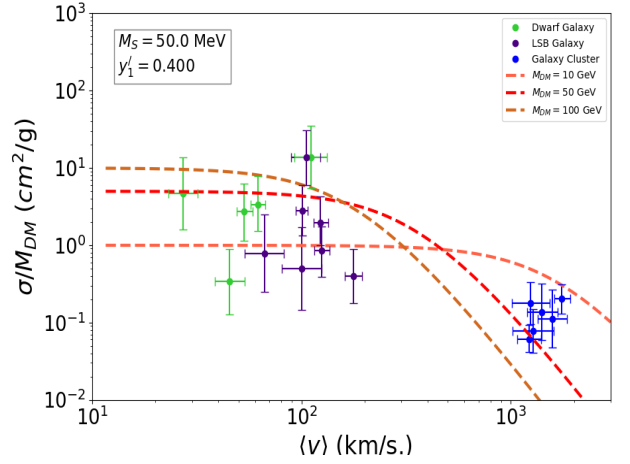


FIG. 11: The self-interaction cross section per unit mass of DM as a function of average collision velocity.

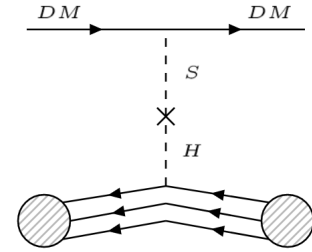


FIG. 12: The spin-independent scattering cross-section of DM-nucleon via Higgs portal.

respectively and they can be given as,

$$f_{p,n} = \sum_{q=u,d,s} f_{T_q}^{p,n} \alpha_q \frac{m_{p,n}}{m_q} + \frac{2}{27} f_{TG}^{p,n} \sum_{q=c,t,b} \alpha_q \frac{m_{p,n}}{m_q}, \quad (21)$$

where

$$\alpha_q = y'_1 \theta_{SH} \left(\frac{m_q}{v} \right) \left[\frac{1}{M_S^2} - \frac{1}{M_H^2} \right]. \quad (22)$$

In Eq. (21), the values of $f_{T_q}^{p,n}$ can be found in [84] and the mixing angle θ_{SH} can be derived in terms of the parameters $\lambda_{SH}, \langle S \rangle, v, M_S, M_h$. Depending on the value of λ_{SH} the $S - H$ mixing can be very small or large. Note that θ_{SH} also has upper bound by invisible Higgs decay (as the singlet scalar is typically lighter than the Higgs mass), while a lower bound on θ_{SH} can be obtained by considering S to decay before the big bang nucleosynthesis (BBN) epoch, *i.e.* $\tau_S < \tau_{\text{BBN}}$. In Fig. 13, we have shown the lower bound on θ_{SH} as a function of M_S from this lifetime criteria. We see from Fig.13 that $\theta_{SH} < 10^{-11}$ is disfavoured for all $M_S \sim 10 \text{ MeV}$.

Using Eq. (21) and (22), the spin-independent cross-

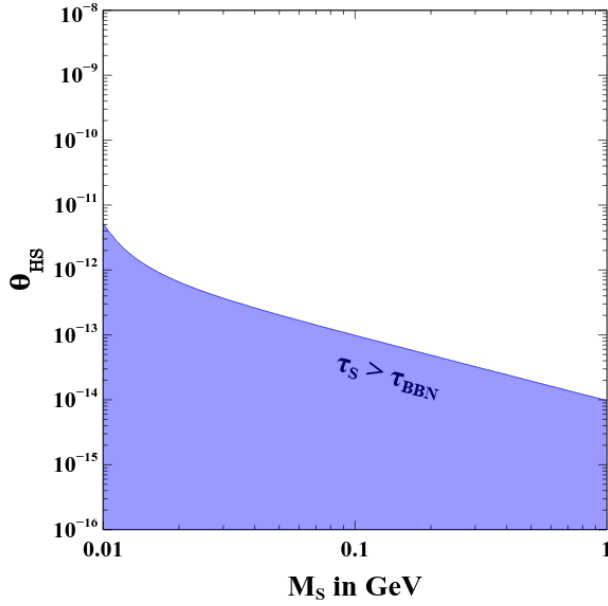


FIG. 13: Lifetime of S is shown in the plane of θ_{SH} versus M_S .

section in Eq. (20), can be re-expressed as:

$$\begin{aligned} \sigma_{SI}^{S-H} &= \frac{\mu_r^2 y_1'^2 \theta_{SH}^2}{\pi A^2} \left[\frac{1}{M_S^2} - \frac{1}{M_H^2} \right]^2 \\ &\times \left[Z \left(\frac{m_p}{v} \right) \left(f_{Tu}^p + f_{Td}^p + f_{Ts}^p + \frac{2}{9} f_{TG}^p \right) \right. \\ &\left. + (A - Z) \left(\frac{m_n}{v} \right) \left(f_{Tu}^n + f_{Td}^n + f_{Ts}^n + \frac{2}{9} f_{TG}^n \right) \right]^2. \end{aligned} \quad (23)$$

Direct search experiments like CRESST-III [85] and XENON1T [86] put severe constraints on the model parameters. XENON1T provides the most stringent constraint on DM mass above 10 GeV, while CRESST constrains the mass regime below 10 GeV. In Fig. 14. The most stringent constraints from CRESST-III [85], XENON1T [86] experiments on $M_{DM} - M_S$ plane are shown against the self-interaction favoured parameter space assuming $y_1' = 0.35$. The blue (purple) coloured contours denote exclusion limits from XENON1T (CRESST-III) experiment for specific $S - H$ mixing parameter θ_{SH} . The region below each contour is excluded for that particular θ_{SH} as shown in the Fig. 14. It is seen that direct search experiments severely constrain the allowed parameter space for self-interaction. In particular, for $M_{DM} = 50$ GeV and $M_S = 50$ MeV, $\theta_{SH} > 10^{-7}$ is already ruled out.

VIII. INDIRECT DETECTION

Now we briefly discuss about the indirect detection prospects and relevant constraints for the model consid-

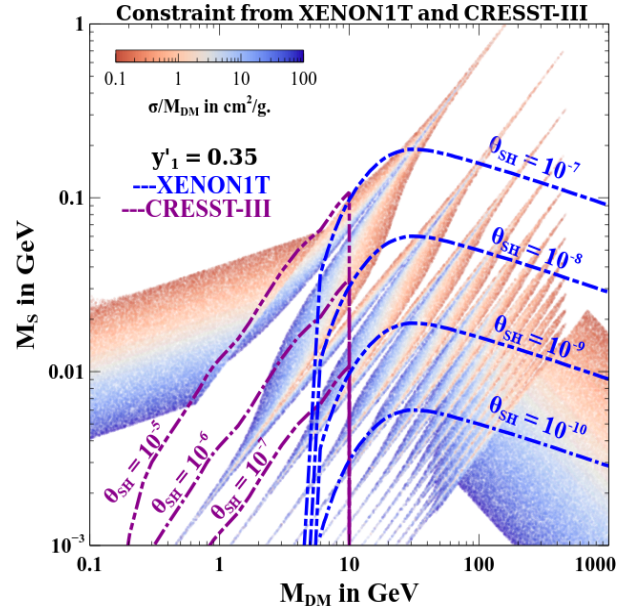


FIG. 14: Constraints from DM direct detection in the plane of DM mass (M_{DM}) versus mediator mass (M_S) for self-interaction.

ered here. Being p-wave process, all the annihilation channels of DM in this model are velocity suppressed ($\sigma v \sim v^2$), unlike a S-wave process, where the cross-section is independent of velocity ($\sigma v \sim v^0$). Since we are considering the mediator S to be very light for sufficient self-interaction, the annihilation cross-section must be multiplied by the Sommerfeld enhancement factor [70], which reflects the modification of the initial-state wave function due to multiple mediator exchange: $(\sigma v)_{\text{enh}} = S \times \sigma v$. The Sommerfeld enhancement factors for s-wave and p-wave annihilations are given respectively as [71–73],

$$\begin{aligned} S_s &= \frac{\pi}{a} \frac{\sinh(2\pi ac)}{\cosh(2\pi ac) - \cos(2\pi\sqrt{c - (ac)^2})} \\ S_p &= \frac{(c - 1)^2 + 4(ac)^2}{1 + 4(ac)^2} S_s \end{aligned} \quad (24)$$

where $a = 2\pi v/y_1'^2$ and $c = 3y_1'^2 M_{DM}/2\pi^3 M_S$

Note that, for $v \gtrsim \frac{y_1'^2}{4\pi}$, we get $S_{s,p} \approx 1$ (and hence not significant at the epoch of DM freeze-out), whereas for smaller velocities S increases proportionally to $1/v$ in the s-wave case and $1/v^3$ in the p-wave case, so that effectively all DM annihilation cross sections (e.g. Eq. 14) increases proportionally to $1/v$ with decreasing velocity in both the cases. The Sommerfeld enhancement saturates for $v \lesssim M_S/(2M_{DM})$, so the ratio of the two masses determines the maximum possible enhancement. Since all the annihilation channels to SM final states are further suppressed by the scalar mixing θ_{SH} (so that $\langle \sigma v \rangle_{DM \rightarrow SM} \sim \theta_{SH}^2/v$), all fluxes of gamma rays, cosmic rays and neutrinos produced by such a set-up are well below the present and future reach of indirect de-

tection probes [69], even in presence of maximum Sommerfeld enhancement. For example, we have estimated that, the benchmark values of the parameters ($M_{\text{DM}} = 100$ GeV, $M_S = 10$ MeV, $y' = 0.35$, $\theta_{SH} \sim 10^{-7}$) considered here gives Sommerfeld enhancement of $\mathcal{O}(10^4)$ and an effective cross-section of $\mathcal{O}(10^{-40})\text{cm}^3/\text{s}$ for the local galactic DM velocity $v = 240 \text{ km/s} = 8 \times 10^{-4}c$, which is well below the current constraints given by the indirect search experiments like Fermi-LAT [74, 75], MAGIC [76], HESS [77], AMS-02 [78], constraints from CMB by Planck [1] and γ -rays by INTEGRAL [79].

IX. COLLIDER SIGNATURES

The fermionic singlet-doublet DM model is rich in collider phenomenology with several interesting signatures such as opposite sign dilepton + missing energy ($\ell^+\ell^- + E_T$), three leptons + missing energy ($\ell\ell\ell + E_T$) etc [57, 60, 87]. Here we briefly point out an interesting feature of the model: the displaced vertex signature of ψ^\pm . Note that the doublet mass required to obtain the correct DM relic density (see Fig. 7) is above $\mathcal{O}(10$ TeV). It is not possible to produce such a heavy particle currently at LHC. However, it can be produced at proposed HE-LHC [88] with 27 TeV centre-of-mass energy and FCC-hh [89] with 100 TeV centre-of-mass energy. Once these particles are produced by virtue of gauge interactions, they can be long-lived before decaying into final state particles including DM [51, 56, 57, 60, 90]. The charged component of the doublet, ψ^\pm may have a sufficiently long lifetime leading to a displaced vertex signature if produced at colliders. The final states of such displaced vertex in forms of charged leptons or jets can be reconstructed by dedicated analysis, some of which in the context of the Large hadron collider (LHC) may be found in [91, 91, 92]. Similar analysis in the context of upcoming experiments like MATHUSLA, electron-proton collider and FCC may be found in [93–96] and references therein.

In the present case, $M_{\psi^0} \gg M_W^1$, so the heavy charged states ψ^\pm can decay directly into a W^\pm and the singlets ($\psi^\pm \rightarrow W^\pm N_{R_i}$) which is suppressed by the tiny singlet-doublet mixing. Importantly, a mass splitting between the charged component of the doublet ψ^\pm and the neutral component ψ^0 can be created from quantum corrections at one loop with virtual photon and Z boson exchange. Virtual W^\pm bosons do not contribute as their couplings to ψ^\pm and ψ^0 are identical. This mass splitting is given by [98, 99],

$$\delta m = |M_{\psi^\pm}| - |M_{\psi^0}| = \frac{\alpha}{2} M_Z f \left(\frac{M_{\psi^\pm}^2}{M_Z^2} \right) \quad (25)$$

¹ LEP experiment currently excludes charged doublet mass below 102.5 GeV [97].

where $f(r)$ is the loop function given as,

$$f(r) = \frac{r}{\pi} \int_0^1 dx (2-x) \ln \left[1 + \frac{x}{r\sqrt{(1-x)^2}} \right].$$

where α is the electromagnetic coupling constant. This mass splitting δm is shown as a function of M_{ψ^\pm} in Fig. 15. With this mass splitting, ψ^\pm can decay into

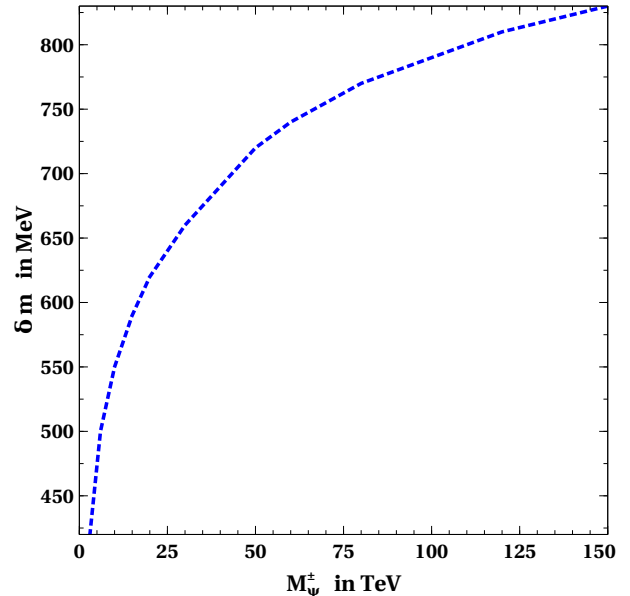


FIG. 15: Mass splitting between ψ^\pm and ψ^0 as a function of M_{ψ^\pm} .

the neutral component ψ^0 and a soft pion via an off-shell W ($\psi^\pm \rightarrow \pi^\pm \psi^0$), which dominates over leptonic decay modes involving $l^\pm \nu$ instead of π^\pm ($\psi^\pm \rightarrow l^\pm \nu \psi^0$) [98]. The possible decay channels of ψ^\pm and the corresponding decay widths are summarised in Appendix D. We see that, unless the Yukawa coupling ($y_i = y$) is larger than 2×10^{-6} , the decay mode $\psi^\pm \rightarrow \pi^\pm \psi^0$ always dominates over other decay channels $\psi^\pm \rightarrow W^\pm N_{R_i}$ as the latter is suppressed by the singlet-doublet mixing. However larger Yukawa coupling will not give the correct relic density as the doublet would decay much early in that case and would lead to under-abundance. So, for the scale of Yukawa coupling that gives correct relic ($y \sim 10^{-10}$), $\psi^\pm \rightarrow \pi^\pm \psi^0$ is the dominant decay mode and its decay width is given by,

$$\Gamma_{\psi^\pm \rightarrow \pi^\pm \psi^0} = \frac{G_F^2}{\pi} (f_\pi \cos \theta_c)^2 \delta m^3 \sqrt{1 - \frac{m_{\pi^\pm}^2}{\delta m^2}}, \quad (26)$$

where, $G_F = 1.16 \times 10^{-5} \text{ GeV}^{-2}$ is the Fermi constant, $f_\pi \approx 135 \text{ MeV}$ is the pion form factor, θ_c is the Cabibbo angle and $m_{\pi^\pm} = 139.57 \text{ MeV}$ is the charged pion mass. We show the corresponding decay length $c\tau_{\psi^\pm}$ in the rest frame of ψ^\pm as a function of M_{ψ^\pm} in Fig. 16. The decay length varies within 0.1-10 cm which gives rise to a displaced vertex signature at colliders. The cyan coloured

region is disallowed from ATLAS search for such long-lived charged particles with a lifetime ranging from 10 ps to 10 ns [100]. As shown in Fig. 7, the doublet mass below 3 TeV can not give rise to correct DM relic density. We exclude these ψ^\pm mass range as depicted by the magenta coloured region. Such displaced vertex signatures can be probed as a signature of verifiability of the model at present and future colliders.

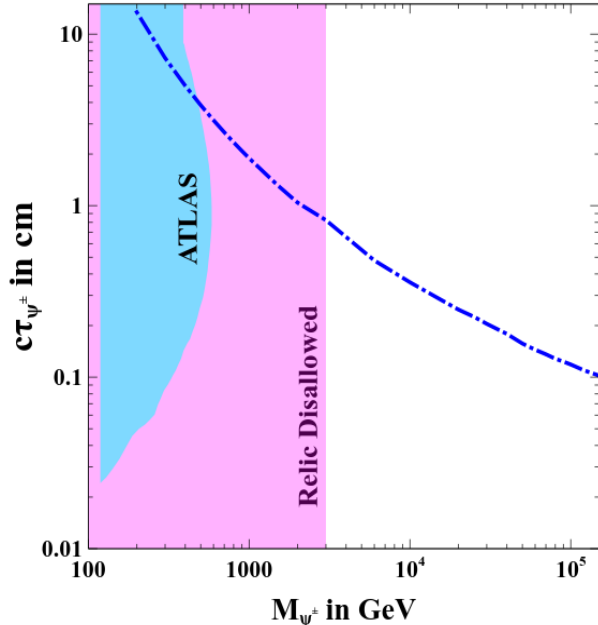


FIG. 16: Decay length of ψ^\pm in its rest frame as a function of M_{ψ^\pm}

X. CONCLUSION

We have studied a singlet-doublet fermion dark matter model to explain the self-interacting nature of dark matter and sub-eV masses of light neutrinos simultaneously. We extended the SM with a vector-like fermion doublet and three right-handed neutrinos (RHNs), all odd under an imposed \mathcal{Z}_2 symmetry. We assumed a negligible mixing between the fermion singlet and fermion doublet in order to keep the doublet long-lived. Moreover, the singlet RHNs are much lighter than the doublet so that the lightest RHN serves as a candidate of DM. Light scalar S ($M_S < M_{DM}$) having sizeable Yukawa coupling ($\sim \mathcal{O}(0.1)$) with the DM not only facilitates velocity-dependent DM self-interaction that helps alleviating the small-scale anomalies of Λ CDM, but also mixes with the SM Higgs providing a portal for detecting such SIDM at terrestrial direct search laboratories. We show that for a typical SIDM of mass 50 GeV and a mediator mass 50 MeV, direct detection experiments like XENON1T and CRESST-III already rule out scalar portal mixing $\theta_{SH} > 10^{-7}$. Due to the large coupling of DM with the

mediator, the thermal relic of the dark matter is negligibly small as DM annihilates efficiently into the light mediator. However, due to the small mixing between the singlet and doublet fermions, the thermal relic of long-lived fermion doublet gets converted into singlet DM at late epochs, typically before the BBN but after the thermal freeze-out of SIDM. The doublet is required to be very heavy in order to generate the correct DM relic density and can be pair-produced at future collider experiments such as HE-LHC and FCC-hh, the decay of which may give rise to displaced vertices. All annihilation channels being p-wave suppressed, the model is also safe from bounds by the indirect detection experiments even in presence of Sommerfeld enhancement due to multiple mediator exchanges. While the lightest RHN is the SIDM, three copies of RHNs along with a \mathcal{Z}_2 -odd scalar doublet can lead to the generation of light neutrino mass at a one-loop level. These \mathcal{Z}_2 -odd particles, apart from their typical contributions to charged lepton flavour violating signatures, can also play an interesting role in DM relic evolution as discussed in this work.

Acknowledgments

MD acknowledges Department of Science and Technology (DST), Govt. of India, for providing the financial assistance for the research under the grant DST/INSPIRE/03/2017/000032. NS acknowledges the support from Department of Atomic Energy (DAE)-Board of Research in Nuclear Sciences (BRNS), Government of India (Ref. Number: 58/14/15/2021-BRNS/37220).

Appendix A: Interactions for DM relic calculations

Gauge interaction of Ψ with SM is given by:

$$\begin{aligned} \mathcal{L}_{int}^\Psi &= \bar{\Psi} i \gamma^\mu \left(-i \frac{g}{2} \tau W_\mu - i g' \frac{Y}{2} B_\mu \right) \Psi \\ &= \left(\frac{e}{2 \sin \theta_W \cos \theta_W} \right) \bar{\psi}^0 \gamma^\mu Z_\mu \psi^0 \\ &\quad + \frac{e}{\sqrt{2} \sin \theta_W} (\bar{\psi}^0 \gamma^\mu W_\mu^+ \psi^- + \psi^+ \gamma^\mu W_\mu^- \psi^0) \quad (\text{A1}) \\ &\quad - e \psi^+ \gamma^\mu A_\mu \psi^- \\ &\quad - \left(\frac{e \cos 2\theta_W}{2 \sin \theta_W \cos \theta_W} \right) \psi^+ \gamma^\mu Z_\mu \psi^-. \end{aligned}$$

where $g = \frac{e}{\sin \theta_W}$ and $g' = \frac{e}{\cos \theta_W}$, e being the electromagnetic coupling constant and θ_W , the Weinberg angle.

Appendix B: DM Self-interaction cross sections at low energy

In the Born Limit ($y_1'^2 M_{DM}/(4\pi M_S) \ll 1$),

$$\sigma_T^{Born} = \frac{y_1'^4}{2\pi M_{DM}^2 v^4} \left(\ln\left(1 + \frac{M_{DM}^2 v^2}{M_S^2}\right) - \frac{M_{DM}^2 v^2}{M_S^2 + M_{DM}^2 v^2} \right) \quad (\text{B1})$$

Outside the Born regime ($y_1'^2 M_{DM}/(4\pi M_S) \geq 1$), there are two distinct regions *viz.*, the classical regime and the resonance regime. In the classical regime ($y_1'^2 M_{DM}/4\pi M_S \geq 1, M_{DM}v/M_S \geq 1$), the solutions for an attractive potential is given by [20, 101, 102]:

$$\sigma_T^{classical} = \begin{cases} \frac{4\pi}{M_S^2} \beta^2 \ln(1 + \beta^{-1}) & \beta \leq 10^{-1} \\ \frac{8\pi}{M_S^2} \beta^2 / (1 + 1.5\beta^{1.65}) & 10^{-1} \leq \beta \leq 10^3 \\ \frac{\pi}{M_S^2} (\ln\beta + 1 - \frac{1}{2}\ln^{-1}\beta) & \beta \geq 10^3 \end{cases} \quad (\text{B2})$$

where $\beta = 2y_1'^2 M_{NR}/(4\pi M_S)v^2$.

Outside the classical regime, there lies the resonant regime for ($y_1'^2 M_{DM}/(4\pi M_S) \geq 1, M_{DM}v/M_S \leq 1$), characterised by the appearance of quantum mechani-

cal resonances and anti-resonance in σ_T due to (quasi-)bound states formation in the attractive potential. No analytical formula for σ_T is available in this regime and the non-relativistic Schrodinger equation needs to be solved by partial wave analysis. Instead, here we use the non-perturbative results obtained by approximating the Yukawa potential to be a Hulthen potential ($V(r) = \pm \frac{y_1'^2}{4\pi} \frac{\delta e^{-\delta r}}{1 - e^{-\delta r}}$), which is given by [20]:

$$\sigma_T^{Hulthen} = \frac{16\pi \sin^2 \delta_0}{M_{DM}^2 v^2} \quad (\text{B3})$$

where $l = 0$ phase shift δ_0 is given in terms of the Γ functions by :

$$\delta_0 = \arg \left(i\Gamma \left(\frac{iM_{DM}v}{k M_S} \right) / \Gamma(\lambda_+) \Gamma(\lambda_-) \right)$$

$$\lambda_{\pm} = 1 + \frac{iM_{DM}v}{2k M_S} \pm \sqrt{\frac{\alpha_D M_{DM}}{k M_S} - \frac{M_{DM}^2 v^2}{4k^2 M_S^2}} \quad (\text{B4})$$

and $k \approx 1.6$ is a dimensionless number.

Appendix C: Relevant cross-sections and decay widths for relic density calculation

$$\Gamma(\Psi \rightarrow H N_i) = \frac{y_i^2}{32\pi M_{\Psi}^3} ((M_{\Psi} + M_{N_i})^2 - M_H^2) \quad (\text{C1})$$

$$\times (M_{\Psi}^4 + M_{N_i}^4 + M_H^4 - 2M_{\Psi}^2 M_{N_i}^2 - 2M_{N_i}^2 M_H^2 - 2M_{\Psi}^2 M_H^2)^{\frac{1}{2}}$$

$$\Gamma(\eta \rightarrow N_i l) \approx \frac{Y_{\alpha i}^2}{32\pi} M_{\eta} \left(1 - 4 \frac{M_{N_i}^2}{M_{\eta}^2}\right)^{3/2} \quad (\text{C2})$$

$$\Gamma(N_{2,3} \rightarrow N_1 l l) \approx \frac{Y_{\alpha 1}^2 Y_{\alpha 2,3}^2 (\Delta M_{2,3})^5}{8\pi M_{\eta}^4} \quad (\text{ where } \Delta M_{2,3} = M_{N_{2,3}} - M_{N_1} \text{).} \quad (\text{C3})$$

$$\sigma(N_i N_i \rightarrow SS) = \frac{y_i^4}{192\pi s (s - 4M_{N_i}^2)} \times \left[\frac{24s(4M_{N_i}^4 + 2M_S^4 + sM_{N_i}^2)A}{M_S^4 + M_{N_i}^2 s - 4M_S^2 M_{N_i}^2} \right. \\ \left. - \frac{24(8M_{N_i}^2 - 4M_S^2 - s^2 - (s - 2M_S^2)4M_{N_i}^2)}{s - 2M_S^2} \text{Log} \left[\frac{2M_S^2 + s(A - 1)}{2M_S^2 - s(A + 1)} \right] \right] \quad (\text{C4})$$

where $A = \sqrt{\frac{(s - 4M_S^2)(s - 4M_{N_i}^2)}{s^2}}$. Thermal averaged cross-section for annihilation of A to B is given by: [82]

$$\langle \sigma v \rangle_{AA \rightarrow BB} = \frac{x}{2[K_1^2(x) + K_2^2(x)]} \times \int_2^{\infty} dz \sigma_{(AA \rightarrow BB)}(z^2 - 4) z^2 K_1(zx) \quad (\text{C5})$$

where $z = \sqrt{s}/M_A$ and $x = M_A/T$. Thermal averaged decay width of A decaying to BC is given by:

$$\langle \Gamma(A \rightarrow BC) \rangle = \Gamma(A \rightarrow BC) \left(\frac{K_1(x)}{K_2(x)} \right) \quad (\text{C6})$$

In Eqn. (C5) and (C6), K_1 and K_2 are the modified Bessel functions of 1st and 2nd kind respectively.

Appendix D: Possible decay modes of ψ^\pm

The decay widths of possible decay modes of ψ^\pm are [57, 98],

$$\Gamma_{\psi^\pm \rightarrow \pi^\pm \psi^0} = \frac{G_F^2}{\pi} (f_\pi \cos \theta_c)^2 \delta m^3 \sqrt{1 - \frac{m_{\pi^\pm}^2}{\delta m^2}}, \quad (\text{D1})$$

$$\Gamma_{\psi^\pm \rightarrow \psi^0 l^\pm \nu} = \frac{G_F^2}{15\pi^3} \delta m^5 \sqrt{1 - b_l^2} P(b_l), \quad (\text{D2})$$

$$\Gamma_{\psi^\pm \rightarrow \pi^\pm N_{R_i}} \approx 2y_i^2 v^2 \frac{G_F^2}{\pi} (f_\pi \cos \theta_c)^2 \Delta M_i \sqrt{1 - \frac{m_{\pi^\pm}^2}{\Delta M_i^2}}, \quad (\text{D3})$$

$$\Gamma_{\psi^\pm \rightarrow W^\pm N_{R_i}} \approx \frac{\alpha y_i^2 v^2}{32s_W^2} \sqrt{\lambda(M_{\psi^\pm}^2, M_{N_{R_i}}^2, M_W^2)} \frac{\left((M_{\psi^\pm} + M_{N_{R_i}}^2 + 2M_W^2) \left((M_{\psi^\pm} - M_{N_{R_i}})^2 - M_W^2 \right) \right)}{M_{\psi^\pm}^3 M_W^2 (M_{\psi^0} - M_{N_{R_i}})^2} \quad (\text{D4})$$

where, $P(b_l) = 1 - \frac{9}{2}b_l^2 - 4b_l^4 + \frac{15b_l^4}{2\sqrt{1-b_l^2}} \tanh^{-1} \sqrt{1-b_l^2}$, $b_l = m_l/\delta m$,

$\lambda(a, b, c) = a^2 + b^2 + c^2 - 2ab - 2ac - 2bc$, $G_F = 1.16 \times 10^{-5} \text{ GeV}^{-2}$ is the Fermi constant, $f_\pi \approx 135 \text{ MeV}$ is the pion form factor, α is electromagnetic coupling constant, θ_c is the Cabibbo angle, $v = 246 \text{ GeV}$ is the vacuum expectation value (vev), s_W is the sin of Weinberg angle, $\delta m = M_{\psi^\pm} - M_{\psi^0}$, $\Delta M_i = M_{\psi^\pm} - M_{N_{R_i}}$, M_W is the mass of W boson and $m_{\pi^\pm} = 139.57 \text{ MeV}$ is the charged pion mass.

Appendix E: Details of CLFV Decay $\mu \rightarrow 3e$

$$\text{Br}(\mu \rightarrow e\bar{e}e) = \frac{3(4\pi)^2 \alpha^2}{8G_F^2} M^2 \text{Br}(\mu \rightarrow e\nu_\mu \bar{\nu}_e) \quad (\text{E1})$$

$$(\text{E2})$$

where M^2 is given as:

$$M^2 = \left[|A_{ND}|^2 + |A_D|^2 \left(\frac{16}{3} \log \left(\frac{m_\mu}{m_e} \right) - \frac{22}{3} \right) + \frac{1}{6} |B|^2 \right. \\ \left. + \frac{1}{3} (2|F_{RR}|^2 + |F_{RL}|^2) + \left(-2A_{ND}A_D^* + \frac{1}{3}A_{ND}B^* - \frac{2}{3}A_DB^* + \text{h.c.} \right) \right] \quad (\text{E3})$$

where A_D is as given in Eq. 10, and A_{ND} is given by:

$$A_{ND} = \sum_{k=1}^3 \frac{(Y)_{ke}^* (Y)_{k\mu}}{6(4\pi)^2} \frac{1}{M_{\eta^+}^2} G_2(r_k), \quad (\text{E4})$$

and

$$F_{RR} = \frac{F g_R^\ell}{g_2^2 \sin^2 \theta_W M_Z^2}, \quad F_{RL} = \frac{F g_L^\ell}{g_2^2 \sin^2 \theta_W M_Z^2}, \quad (\text{E5})$$

with the co-efficient F given by

$$F = \sum_{k=1}^3 \frac{(Y)_{ke}^* (Y)_{k\mu}}{2(4\pi)^2} \frac{m_\mu m_e}{M_{\eta^+}^2} \frac{g_2}{\cos \theta_W} F_2(r_k). \quad (\text{E6})$$

For the Box diagrams, the co-efficient B is given by:

$$B = \frac{1}{(4\pi)^2 e^2 M_{\eta^+}^2} \sum_{j,k=1}^3 \left[\frac{1}{2} D_1(r_j, r_k) (Y)_{ke}^* (Y)_{ke} (Y)_{je}^* (Y)_{j\mu} + \sqrt{r_j r_k} D_2(r_j, r_k) (Y)_{ke}^* (Y)_{ke}^* (Y)_{je} (Y)_{j\mu} \right]. \quad (\text{E7})$$

The loop functions G_2, F_2, D_1, D_2 are given by:

$$F_2(x) = \frac{1 - 6x + 3x^2 + 2x^3 - 6x^2 \log x}{6(1-x)^4}, \quad (\text{E8})$$

$$G_2(x) = \frac{2 - 9x + 18x^2 - 11x^3 + 6x^3 \log x}{6(1-x)^4}, \quad (\text{E9})$$

$$D_1(x, y) = -\frac{1}{(1-x)(1-y)} - \frac{x^2 \log x}{(1-x)^2(x-y)} - \frac{y^2 \log y}{(1-y)^2(y-x)}, \quad (\text{E10})$$

$$D_2(x, y) = -\frac{1}{(1-x)(1-y)} - \frac{x \log x}{(1-x)^2(x-y)} - \frac{y \log y}{(1-y)^2(y-x)}. \quad (\text{E11})$$

These loop functions do not have any poles. In the limit $x, y \rightarrow 1$ and $y \rightarrow x$, the functions become

$$F_2(1) = \frac{1}{12}, \quad G_2(1) = \frac{1}{4}, \quad D_1(1, 1) = -\frac{1}{3}, \quad D_2(1, 1) = \frac{1}{6}, \quad (\text{E12})$$

$$D_1(x, x) = \frac{-1 + x^2 - 2x \log x}{(1-x)^3}, \quad D_1(x, 1) = D_1(1, x) = \frac{-1 + 4x - 3x^2 + 2x^2 \log x}{2(1-x)^3}, \quad (\text{E13})$$

$$D_2(x, x) = \frac{-2 + 2x - (1+x) \log x}{(1-x)^3}, \quad D_2(x, 1) = D_2(1, x) = \frac{1 - x^2 + 2x \log x}{2(1-x)^3}. \quad (\text{E14})$$

Appendix F: Details of $\mu \rightarrow e$ conversion in nuclei

$$\text{CR}(\mu \rightarrow e, \text{Nucleus}) = \frac{p_e E_e m_\mu^3 G_F^2 \alpha_{\text{em}}^3 Z_{\text{eff}}^4 F_p^2 K^2}{8\pi^2 Z} \frac{1}{\Gamma_{\text{capt}}}. \quad (\text{F1})$$

where

$$K^2 = \left| (Z+N) \left(g_{LV}^{(0)} + g_{LS}^{(0)} \right) + (Z-N) \left(g_{LV}^{(1)} + g_{LS}^{(1)} \right) \right|^2 + \left| (Z+N) \left(g_{RV}^{(0)} + g_{RS}^{(0)} \right) + (Z-N) \left(g_{RV}^{(1)} + g_{RS}^{(1)} \right) \right|^2 \quad (\text{F2})$$

In the above, $g_{XK}^{(0)}$ and $g_{XK}^{(1)}$ (with $X = L, R$ and $K = S, V$) are given by

$$g_{XK}^{(0)} = \frac{1}{2} \sum_{q=u,d,s} \left(g_{XK(q)} G_K^{(q,p)} + g_{XK(q)} G_K^{(q,n)} \right), \quad g_{XK}^{(1)} = \frac{1}{2} \sum_{q=u,d,s} \left(g_{XK(q)} G_K^{(q,p)} - g_{XK(q)} G_K^{(q,n)} \right). \quad (\text{F3})$$

Neglecting the Higgs-penguin contributions due to the smallness of the involved Yukawa couplings. Therefore, the corresponding couplings are

$$g_{LV(q)} = g_{LV(q)}^\gamma + g_{LV(q)}^Z, \quad g_{RV(q)} = g_{LV(q)} \Big|_{L \leftrightarrow R}, \quad g_{LS(q)} \approx 0, \quad g_{RS(q)} \approx 0. \quad (\text{F4})$$

The photon and Z -boson couplings can be computed from the Feynman diagrams which are given by:

$$g_{LV(q)}^\gamma = \frac{\sqrt{2}}{G_F} e^2 Q_q (A_{ND} - A_D), \quad g_{RV(q)}^Z = -\frac{\sqrt{2}}{G_F} \frac{g_L^q + g_R^q}{2} \frac{F}{M_Z^2}. \quad (\text{F5})$$

And the tree-level Z -boson couplings to a pair of quarks are:

$$g_L^q = \frac{g_2}{\cos \theta_W} (Q_q \sin^2 \theta_W - T_3^q), \quad g_R^q = \frac{g_2}{\cos \theta_W} Q_q \sin^2 \theta_W, \quad (\text{F6})$$

[1] N. Aghanim et al. (Planck) (2018), 1807.06209.

[2] F. Zwicky, Helv. Phys. Acta **6**, 110 (1933), [Gen. Rel.

- Grav.41,207(2009)].
- [3] V. C. Rubin and W. K. Ford, Jr., *Astrophys. J.* **159**, 379 (1970).
 - [4] D. Clowe, M. Bradac, A. H. Gonzalez, M. Markevitch, S. W. Randall, C. Jones, and D. Zaritsky, *Astrophys. J.* **648**, L109 (2006), astro-ph/0608407.
 - [5] E. W. Kolb and M. S. Turner, *The Early Universe*, vol. 69 (1990), ISBN 978-0-201-62674-2.
 - [6] S. Tulin and H.-B. Yu, *Phys. Rept.* **730**, 1 (2018), 1705.02358.
 - [7] J. S. Bullock and M. Boylan-Kolchin, *Ann. Rev. Astron. Astrophys.* **55**, 343 (2017), 1707.04256.
 - [8] D. N. Spergel and P. J. Steinhardt, *Phys. Rev. Lett.* **84**, 3760 (2000), astro-ph/9909386.
 - [9] E. D. Carlson, M. E. Machacek, and L. J. Hall, *Astrophys. J.* **398**, 43 (1992).
 - [10] A. A. de Laix, R. J. Scherrer, and R. K. Schaefer, *Astrophys. J.* **452**, 495 (1995), astro-ph/9502087.
 - [11] M. R. Buckley and P. J. Fox, *Phys. Rev. D* **81**, 083522 (2010), 0911.3898.
 - [12] J. L. Feng, M. Kaplinghat, and H.-B. Yu, *Phys. Rev. Lett.* **104**, 151301 (2010), 0911.0422.
 - [13] J. L. Feng, M. Kaplinghat, H. Tu, and H.-B. Yu, *JCAP* **07**, 004 (2009), 0905.3039.
 - [14] A. Loeb and N. Weiner, *Phys. Rev. Lett.* **106**, 171302 (2011), 1011.6374.
 - [15] J. Zavala, M. Vogelsberger, and M. G. Walker, *Mon. Not. Roy. Astron. Soc.* **431**, L20 (2013), 1211.6426.
 - [16] M. Vogelsberger, J. Zavala, and A. Loeb, *Mon. Not. Roy. Astron. Soc.* **423**, 3740 (2012), 1201.5892.
 - [17] T. Bringmann, F. Kahlhoefer, K. Schmidt-Hoberg, and P. Walia, *Phys. Rev. Lett.* **118**, 141802 (2017), 1612.00845.
 - [18] M. Kaplinghat, S. Tulin, and H.-B. Yu, *Phys. Rev. Lett.* **116**, 041302 (2016), 1508.03339.
 - [19] L. G. van den Aarssen, T. Bringmann, and C. Pfrommer, *Phys. Rev. Lett.* **109**, 231301 (2012), 1205.5809.
 - [20] S. Tulin, H.-B. Yu, and K. M. Zurek, *Phys. Rev. D* **87**, 115007 (2013), 1302.3898.
 - [21] M. Kaplinghat, S. Tulin, and H.-B. Yu, *Phys. Rev. D* **89**, 035009 (2014), 1310.7945.
 - [22] E. Del Nobile, M. Kaplinghat, and H.-B. Yu, *JCAP* **10**, 055 (2015), 1507.04007.
 - [23] C. Kouvaris, I. M. Shoemaker, and K. Tuominen, *Phys. Rev. D* **91**, 043519 (2015), 1411.3730.
 - [24] N. Bernal, X. Chu, C. Garcia-Cely, T. Hambye, and B. Zaldivar, *JCAP* **03**, 018 (2016), 1510.08063.
 - [25] K. Kainulainen, K. Tuominen, and V. Vaskonen, *Phys. Rev. D* **93**, 015016 (2016), [Erratum: *Phys.Rev.D* 95, 079901 (2017)], 1507.04931.
 - [26] T. Hambye and L. Vanderheyden, *JCAP* **05**, 001 (2020), 1912.11708.
 - [27] M. Cirelli, P. Panci, K. Petraki, F. Sala, and M. Taoso, *JCAP* **05**, 036 (2017), 1612.07295.
 - [28] F. Kahlhoefer, K. Schmidt-Hoberg, and S. Wild, *JCAP* **08**, 003 (2017), 1704.02149.
 - [29] M. Dutta, S. Mahapatra, D. Borah, and N. Sahu (2021), 2101.06472.
 - [30] D. Borah, M. Dutta, S. Mahapatra, and N. Sahu (2021), 2107.13176.
 - [31] D. Borah, M. Dutta, S. Mahapatra, and N. Sahu (2021), 2110.00021.
 - [32] P. A. Zyla et al. (Particle Data Group), *PTEP* **2020**, 083C01 (2020).
 - [33] R. N. Mohapatra et al., *Rept. Prog. Phys.* **70**, 1757 (2007), hep-ph/0510213.
 - [34] A. Freitas, S. Westhoff, and J. Zupan, *JHEP* **09**, 015 (2015), 1506.04149.
 - [35] G. Cynolter, J. Kovács, and E. Lendvai, *Mod. Phys. Lett.* **A31**, 1650013 (2016), 1509.05323.
 - [36] L. Calibbi, A. Mariotti, and P. Tziveloglou, *JHEP* **10**, 116 (2015), 1505.03867.
 - [37] T. Abe, R. Kitano, and R. Sato, *Phys. Rev. D* **91**, 095004 (2015), [Erratum: *Phys.Rev.D* 96, 019902 (2017)], 1411.1335.
 - [38] C. Cheung and D. Sanford, *JCAP* **1402**, 011 (2014), 1311.5896.
 - [39] T. Cohen, J. Kearney, A. Pierce, and D. Tucker-Smith, *Phys. Rev.* **D85**, 075003 (2012), 1109.2604.
 - [40] R. Enberg, P. J. Fox, L. J. Hall, A. Y. Papaioannou, and M. Papucci, *JHEP* **11**, 014 (2007), 0706.0918.
 - [41] F. D’Eramo, *Phys. Rev.* **D76**, 083522 (2007), 0705.4493.
 - [42] S. Banerjee, S. Matsumoto, K. Mukaida, and Y.-L. S. Tsai, *JHEP* **11**, 070 (2016), 1603.07387.
 - [43] A. Dutta Banik, A. K. Saha, and A. Sil, *Phys. Rev.* **D98**, 075013 (2018), 1806.08080.
 - [44] S. Horiuchi, O. Macias, D. Restrepo, A. Rivera, O. Zapata, and H. Silverwood, *JCAP* **03**, 048 (2016), 1602.04788.
 - [45] D. Restrepo, A. Rivera, M. Sánchez-Peláez, O. Zapata, and W. Tangarife, *Phys. Rev.* **D92**, 013005 (2015), 1504.07892.
 - [46] M. Badziak, M. Olechowski, and P. Szczerbiak, *Phys. Lett. B* **770**, 226 (2017), 1701.05869.
 - [47] A. Betancur, G. Palacio, and A. Rivera (2020), 2002.02036.
 - [48] T. Abe and R. Sato, *Phys. Rev. D* **99**, 035012 (2019), 1901.02278.
 - [49] T. Abe, *Phys. Lett. B* **771**, 125 (2017), 1702.07236.
 - [50] D. Borah, M. Dutta, S. Mahapatra, and N. Sahu (2021), 2109.02699.
 - [51] S. Bhattacharya, N. Sahoo, and N. Sahu, *Phys. Rev.* **D96**, 035010 (2017), 1704.03417.
 - [52] B. Barman, S. Bhattacharya, P. Ghosh, S. Kadam, and N. Sahu, *Phys. Rev. D* **100**, 015027 (2019), 1902.01217.
 - [53] S. Bhattacharya, P. Ghosh, and N. Sahu, *JHEP* **02**, 059 (2019), 1809.07474.
 - [54] S. Bhattacharya, B. Karmakar, N. Sahu, and A. Sil, *JHEP* **05**, 068 (2017), 1611.07419.
 - [55] S. Bhattacharya, N. Sahoo, and N. Sahu, *Phys. Rev. D* **93**, 115040 (2016), 1510.02760.
 - [56] S. Bhattacharya, P. Ghosh, N. Sahoo, and N. Sahu (2018), 1812.06505.
 - [57] L. Calibbi, L. Lopez-Honorez, S. Lowette, and A. Mariotti, *JHEP* **09**, 037 (2018), 1805.04423.
 - [58] P. Konar, A. Mukherjee, A. K. Saha, and S. Show, *Phys. Rev. D* **102**, 015024 (2020), 2001.11325.
 - [59] P. Konar, A. Mukherjee, A. K. Saha, and S. Show, *JHEP* **03**, 044 (2021), 2007.15608.
 - [60] M. Dutta, S. Bhattacharya, P. Ghosh, and N. Sahu, *JCAP* **03**, 008 (2021), 2009.00885.
 - [61] M. Dutta, S. Bhattacharya, P. Ghosh, and N. Sahu, in *24th DAE-BRNS High Energy Physics Symposium* (2021), 2106.13857.
 - [62] E. Ma, *Phys. Rev.* **D73**, 077301 (2006), hep-ph/0601225.
 - [63] J. A. Casas and A. Ibarra, *Nucl. Phys.* **B618**, 171 (2001), hep-ph/0103065.

- [64] T. Toma and A. Vicente, *JHEP* **01**, 160 (2014), 1312.2840.
- [65] A. M. Baldini et al. (MEG), *Eur. Phys. J.* **C76**, 434 (2016), 1605.05081.
- [66] U. Bellgardt et al. (SINDRUM), *Nucl. Phys. B* **299**, 1–6 (1988).
- [67] C. Dohmen et al. (SINDRUM-II), *Phys. Lett. B* **317**, 631–636 (1993).
- [68] L. Lavoura, *Eur. Phys. J.* **C29**, 191 (2003), hep-ph/0302221.
- [69] C. Arina, *Front. Astron. Space Sci.* **5**, 30 (2018), 1805.04290.
- [70] A. Sommerfeld, *Annalen der Physik* **403**, 207 (1931).
- [71] S. Cassel, *J. Phys. G* **37**, 105009 (2010), 0903.5307.
- [72] R. Iengo, *JHEP* **05**, 024 (2009), 0902.0688.
- [73] T. R. Slatyer, *JCAP* **02**, 028 (2010), 0910.5713.
- [74] M. Ackermann et al. (Fermi-LAT), *Phys. Rev. Lett.* **115**, 231301 (2015), 1503.02641.
- [75] M. Ackermann et al. (Fermi-LAT), *Phys. Rev. D* **89**, 042001 (2014), 1310.0828.
- [76] M. L. Ahnen et al. (MAGIC, Fermi-LAT), *JCAP* **02**, 039 (2016), 1601.06590.
- [77] H. Abdallah et al. (HESS), *Phys. Rev. Lett.* **120**, 201101 (2018), 1805.05741.
- [78] M. Aguilar et al., *Phys. Rev. Lett.* **110**, 141102 (2013).
- [79] J. Knodlseder, G. Weidenspointner, P. Jean, R. Diehl, A. Strong, H. Halloin, B. Cordier, S. Schanne, and C. Winkler, *ESA Spec. Publ.* **622**, 13 (2007), 0712.1668.
- [80] A. Semenov, *Computer Physics Communications* **115**, 124 (1998), ISSN 0010-4655, computer Algebra in Physics Research.
- [81] G. Belanger, F. Boudjema, A. Pukhov, and A. Semenov, *Comput. Phys. Commun.* **180**, 747 (2009), 0803.2360.
- [82] P. Gondolo and G. Gelmini, *Nucl. Phys.* **B360**, 145 (1991).
- [83] A. Kamada, H. J. Kim, and T. Kuwahara, *JHEP* **20**, 202 (2020), 2007.15522.
- [84] J. R. Ellis, A. Ferstl, and K. A. Olive, *Phys. Lett.* **B481**, 304 (2000), hep-ph/0001005.
- [85] A. Abdelhameed et al. (CRESST), *Phys. Rev. D* **100**, 102002 (2019), 1904.00498.
- [86] E. Aprile et al. (2018), 1805.12562.
- [87] S. Bhattacharya, S. Jahedi, and J. Wudka (2021), 2106.02846.
- [88] A. Abada et al. (FCC), *Eur. Phys. J. ST* **228**, 1109 (2019).
- [89] A. Abada et al. (FCC), *Eur. Phys. J. ST* **228**, 755 (2019).
- [90] D. Borah, D. Nanda, N. Narendra, and N. Sahu (2018), 1810.12920.
- [91] M. Aaboud et al. (ATLAS), *Phys. Rev. D* **93**, 112015 (2016), 1604.04520.
- [92] V. Khachatryan et al. (CMS), *Phys. Rev. D* **94**, 112004 (2016), 1609.08382.
- [93] D. Curtin and M. E. Peskin, *Phys. Rev. D* **97**, 015006 (2018), 1705.06327.
- [94] D. Curtin, K. Deshpande, O. Fischer, and J. Zurita, *JHEP* **07**, 024 (2018), 1712.07135.
- [95] S. Jana, N. Okada, and D. Raut (2020), 1911.09037.
- [96] C. Sen, P. Bandyopadhyay, S. Dutta, and A. KT (2021), 2107.12442.
- [97] J. Abdallah et al. (DELPHI), *Eur. Phys. J. C* **31**, 421 (2003), hep-ex/0311019.
- [98] S. D. Thomas and J. D. Wells, *Phys. Rev. Lett.* **81**, 34 (1998), hep-ph/9804359.
- [99] M. Cirelli and A. Strumia, *New J. Phys.* **11**, 105005 (2009), 0903.3381.
- [100] M. Aaboud et al. (ATLAS), *JHEP* **06**, 022 (2018), 1712.02118.
- [101] S. Tulin, H.-B. Yu, and K. M. Zurek, *Phys. Rev. Lett.* **110**, 111301 (2013), 1210.0900.
- [102] S. A. Khrapak, A. V. Ivlev, G. E. Morfill, and S. K. Zhdanov, *Phys. Rev. Lett.* **90**, 225002 (2003).